Sensitivity of global CO simulations to uncertainties in biomass burning sources

H. Bian,[1,2] M. Chin,[3] S. R. Kawa,[3] B. Duncan,[1,2] A. Arellano,[4] and P. Kasibhatla[5]

[1] One of the largest uncertainties for the modeling of tropospheric carbon monoxide (CO) concentration is the timing, location, and magnitude of biomass burning emissions. We investigate the sensitivity of simulated CO in the Unified Chemistry Transport Model (UCTM) to several biomass burning emissions, including four bottom-up and two top-down inventories. We compare the sensitivity experiments with observations from MOPITT, surface and airborne NOAA Global Monitoring Division network data, and the TRACE-P field campaign. The variation of the global annual emissions of these six biomass burning inventories is within 30%; however, their regional variations are often much higher (factor of 2−5). These uncertainties translate to about 6% variation in the global simulated CO but more than a 100% variation in some regions. The annual mean CO variation is greater in the Southern Hemisphere (>12%) than in the Northern Hemisphere (<5%), largely because biomass burning is a higher percentage of the total source in the Southern Hemisphere. Comparisons with CO observations indicate that each model inventory has its strengths and shortcomings, and these regional variations are examined. Overall the model CO concentrations are within the observed range of variability at most stations including Ascension Island, which is strongly influenced by fire emissions. In addition, we discuss the systematic biases that exist in the inventories developed by the similar methodologies and original satellite data.

Citation: Bian, H., M. Chin, S. R. Kawa, B. Duncan, A. Arellano, and P. Kasibhatla (2007), Sensitivity of global CO simulations to uncertainties in biomass burning sources, *J. Geophys. Res.*, *112*, D23308, doi:10.1029/2006JD008376.

1. Introduction

[2] Carbon monoxide (CO) has been studied extensively because of its important role in atmospheric chemistry, air quality, and carbon research [*Seinfeld*, 1986; *Chameides et al.*, 1994; *Holloway et al.*, 2000; *Pétron et al.*, 2002; *Lamarque et al.*, 2004; *Schmitgen et al.*, 2004; *Suntharalingam et al.*, 2004]. Advancements in the simulation of CO are often driven by improved source estimates. Currently, fossil fuel emission is more or less known in developed countries, but not in developing countries. Biofuel is still not well known in developing countries because of the uncertainties in the fuel use and mixture. Our confidence in estimates of CO from the oxidation of biogenic nonmethane hydrocarbons (NMHC) is low because of uncertainties in vegetation types and chemical degradation pathways. One of the largest uncertainties is in the temporal and spatial variability of biomass burning, a global emission source in the same order as fossil fuels.

[3] Recently, there has been an effort to provide accurate and near real-time biomass burning emissions, using both "bottom-up" and "top-down" approaches. A number of studies used bottom-up method with constraints from satellite fire data to investigate biomass burning over global [*Duncan et al.*, 2003; *van der Werf et al.*, 2003; *Hoelzemann et al.*, 2004; *Ito and Penner*, 2004] and regional scales [*Pfister et al.*, 2004, 2005; *Ito and Penner*, 2005; *Kasischke et al.*, 2005]. For example, *Duncan et al.* [2003] investigated interannual and seasonal variability of biomass burning constrained by observations from Total Ozone Mapping Spectrometer (TOMS), Along Track Scanning Radiometer (ATSR), and A Very High Resolution Radiometer (AVHRR). Biomass burning emissions were also estimated from the Tropical Rainfall Measuring Mission (TRMM), ATSR, AVHRR, and Moderate resolution Imaging Spectrometer (MODIS) [*van der Werf et al.*, 2003, 2006; *Randerson et al.*, 2005]. Although the satellite products provide the key information on timing and location of fires, the quantitative estimate of tracer emissions from biomass burning is still difficult, mainly because of uncertainties in fuel loads, combustion efficiency, and burned area that are used to convert satellite fire data to biomass burning emissions [*van der Werf et al.*, 2006].

[4] A different approach, the top-down method, was developed to refine the bottom-up method by using the

---

[1]Goddard Earth Sciences and Technology Center, University of Maryland, Baltimore County, Baltimore, Maryland, USA.
[2]Also at Atmospheric Chemistry and Dynamics Branch, NASA Goddard Space Flight Center, Greenbelt, Maryland, USA.
[3]Atmospheric Chemistry and Dynamics Branch, NASA Goddard Space Flight Center, Greenbelt, Maryland, USA.
[4]National Center for Atmospheric Research, Boulder, Colorado, USA.
[5]Nicholas School of the Environment and Earth Sciences, Duke University, Durham, North Carolina, USA.

Table 1. Six Biomass Burning Emissions Used in This Study

Name	Description	References
GFED1	Global Fire Emission Database version 1	*van der Werf et al.* [2003, 2004]; *Randerson et al.* [2005]
GFED2	Global Fire Emission Database version 2	*van der Werf et al.* [2006]
Arellano1	global top-down emission with a priori emission of GFED1 and atmospheric constraint from MOPITT	*Arellano et al.* [2004]
Arellano2	based on Arellano1 with an additional atmospheric constraint of GMD ground measurements	*Arellano* [2005]
Duncan1	scaled climatological emission of Duncan2 with measurements of TOMS Aerosol Index and ATSR and AVHRR fire counts	*Duncan et al.* [2003]
Duncan2	climatological emission	*Duncan et al.* [2003]

CO atmospheric observations [*Arellano et al.*, 2004, 2006; *Pétron et al.*, 2002; *Muller and Stavrakou*, 2005; *Heald et al.*, 2004; *Palmer et al.*, 2003; *Pfister et al.*, 2004]. For example, top-down emission inventories were constructed with atmospheric constraints from the total column measurements by the satellite sensor MOPITT [*Arellano et al.*, 2004, 2006] and from the surface measurements in the GMD network [*Arellano*, 2005]. Similar approach was used by *Pfister et al.* [2004] and *Pétron et al.* [2002]. The top-down approach may have a quite difference from the a priori estimates.

[5] Here, we present a study of the differences in CO distributions simulated in a global model due to the differences in biomass burning emissions. We are particularly interested in exploring the sensitivity of CO to the uncertainties in biomass burning emissions for different regions and seasons. We conduct CO simulations using six different biomass burning inventories that are commonly used in tropospheric CO studies [*Heald et al.*, 2003; *Palmer et al.*, 2003; *Allen et al.*, 2004; *Arellano et al.*, 2004, 2006]. These inventories are based on either TOMS/ATSR/AVHRR (TOMS-based [*Duncan et al.*, 2003]) or on TRMM/ATSR/AVHRR/MODIS (TRMM-based [*Randerson et al.*, 2005; *van der Werf et al.*, 2003, 2004, 2006]). Model CO concentrations are compared with various kinds of measurements. Consequently, a recommendation of an optimal choice of biomass burning emission from the six referred inventories is provided over regional scales. Clearly, caution should be taken in the recommendation as will be discussed later in section 3.2 because the difference between simulated and observed CO is not only caused by bias in biomass burning, but also induced by uncertainties in other emissions, chemistry, and transport processes.

[6] We organize this paper as follows. Model framework and measurements are described in sections 2.1, and 2.2 respectively. In particular we present monthly CO biomass burning emissions over seven regions for each of six CO biomass burning inventories and summarize the spatial and temporal discrepancies of the emissions in section 2.1.1. Section 3 discusses the sensitivity of simulated CO to different biomass burning inventories by comparing the model results with surface concentrations from the GMD

network measurements (section 3.1), global column CO from MOPITT satellite retrieval (section 3.2), and vertical profiles from GMD and TRACE-P aircraft measurements (section 3.3). Conclusions and implications of this work are presented in section 4.

2. Model and Measurements

2.1. Model Description

[7] The GSFC unified chemistry transport model (CTM) is described by *Bian et al.* [2006]. This off-line CTM is driven by assimilated meteorological fields of NASA's Goddard Earth Observation System, Version 4 (GEOS-4) data assimilation system (DAS), updated meteorological fields every 3 h [*Bloom et al.*, 2005]. The spatial resolution of the model used in this study is 2° latitude by 2.5° longitude by 25 vertical layers with a model lid of 0.01 hPa; the tropospheric layers are of the same vertical resolution as the meteorological fields.

[8] The advection and diffusion algorithms, which use the same transport core as Goddard Chemistry Aerosol Radiation and Transport (GOCART) [*Chin et al.*, 2002, 2004] and Goddard Parameterized CTM (PCTM) [*Kawa et al.*, 2004], have been extensively evaluated [*Lin and Rood*, 1996; *Li et al.*, 2002; *Douglass et al.*, 2003]. The convection algorithm, which is designed to be consistent with the deep convection scheme [*Zhang and McFarlane*, 1995] and shallow cloud scheme [*Hack*, 1994] used in the underlying GCM, has been evaluated in a recent CO_2 study [*Bian et al.*, 2006].

[9] The six biomass burning inventories are shown in Tables 1 and 2. Other sources of CO are summarized in Table 2. These emissions are explained in the following three subsections.

2.1.1. Alternative Biomass Burning Emissions in Sensitivity Studies

[10] The biomass burning emission inventories in Table 1 are either based on TOMS or TRMM data. The two TOMS-

Table 2. Total CO Emissions

	Direct Emission	Photochemical Oxidation	References
Fossil fuel	351.6	70.3	*Streets et al.* [2003, 2006]; *Palmer et al.* [2003]; *Bey et al.* [2001]
Biofuel	166.4	31.6	*Yevich and Logan* [2003]; *Streets et al.* [2003]; *Palmer et al.* [2003]
Biomass burning			
GFED2	350.7	38.6	see Table 1
GFED1	444.6	48.9	see Table 1
Arellano1	517.5		see Table 1
Arellano2	415.7		see Table 1
Duncan1	403.3	44.4	see Table 1
Duncan2	429.8	47.3	see Table 1
Biogenic			
Isoprene		176.6	*Guenther et al.* [1995]; *Wang et al.* [1998]
Monoterpene		50.1	*Guenther et al.* [1995]; *Wang et al.* [1998]
Methanol		87.4	*Guenther et al.* [1995]; *Wang et al.* [1998]
CH_4 oxidation		789.2	*DeMore et al.* [1997]
Total	962.6[a]	1254.1[a]	

[a]Estimated using GFED1.

based inventories are bottom-up emissions and the TRMM-based emissions include two bottom-up and two top-down emissions. The approaches of bottom-up and top-down are currently the only two methods to obtain emissions. The bottom-up method compiles emission inventories by characterizing vegetation burning and emission factors, while the top-down method infers surface fluxes by modifying a priori emissions using tropospheric CO concentration measurements. The bottom-up method is hampered by limited data [*Streets et al.*, 2006] and the top-down approach is limited by the uncertainty in atmospheric transport [*Gurney et al.*, 2002; *Arellano et al.*, 2004].

[11] The two TOMS-based, bottom-up inventories use the annual CO emission climatology presented by *Duncan et al.* [2003], which considers emissions from deforestation, shifting cultivation, agricultural residues burned in the field, savanna burning, and forest wild fires. The interannual and seasonal variability is estimated using satellite observations. The period of burning in the first inventory is specific to April 2000 to March 2001 (Duncan1) and derived from measurements of the TOMS Aerosol Index (AI) and ATSR fire counts. The seasonal timing of burning in the second is for a mean year and is derived from an average of fire counts from the ATSR and AVHRR World Fire Atlases (Duncan2). The two methods are described by *Duncan et al.* [2003].

[12] The two TRMM-based bottom-up emissions are the Global Fire Emissions Database version 1 (GFED1) and 2 (GFED2). The GFED1 inventory was constructed using the approaches described in *van der Werf et al.* [2003, 2004] and *Randerson et al.* [2005]. The data set is integrated from several satellite products over different locations and time periods. Over regions 38°N–38°S, the data set obtains the relationship of TRMM-VIRS hot spot data and burned area using MODIS burned area tiles across Africa, South America, and Australia. For the study period where MODIS data were not available, the data set uses a separate linear relationship between ATSR and VIRS for each grid cell obtained over the time window when ATSR and TRMM overlapped. In the extratropics, the approach is extended using ATSR data and a combination of country-level fire statistics and AVHRR data in the Russian Far East. The GFED2 inventory is a modified and updated version of GFED1 [*van der Werf et al.*, 2006], which improves burned area and includes organic soil carbon and peatland fuels. These modifications have lowered emissions in southern Africa and South America and raised emissions in boreal regions.

[13] One top-down emission, based on the GFED1, is constrained by MOPITT CO column observations (Arellano1) [*Arellano et al.*, 2004]. Fifteen individual CO source categories are considered, which include fossil fuel/biofuel combustion in seven geographical regions, biomass burning in seven geographical regions, and the global CO source from the oxidation of isoprene and monoterpenes. Response functions for each source category are calculated using the GEOS-CHEM CTM driven by NASA/GMAO assimilated meteorological fields. The other top-down emission is also based on the GFED1 and uses a similar technique approach as in Arellano1, but is constrained first by MOPITT CO and then by GMD ground CO measurements (Arellano2) [*Arellano*, 2005]. The top down approach incorporates long-term and global atmospheric information into the emission estimation and it is expected to give a more realistic emission data set.

[14] An important difference between the top-down and bottom-up approaches is that the estimation of biomass burning emissions from the bottom-up approach is independent from other emissions (e.g., fossil fuels and biofuels). On the other hand, the top-down emission is usually optimized together with fossil fuel and biofuel emissions, especially in Asia where the sources are often colocated. This same issue applies to the source of CO from the oxidation of methane and NMHC, including coemitted NMHC from biomass burning. An additional indirect emission of CO from NMHC oxidation is accounted for in the four bottom-up emissions (see 2.1.3 for details). Nevertheless, the two optimized top-down emissions already include this effect in their emission amounts. In general, the agreement of top-down estimation is strongly constrained by the fact that those were built (using another model) to minimize their distance to atmospheric observations. The constrained emissions using one model might be, however to some extent, used in another model quite successfully [*Arellano and Hess*, 2006].

[15] Figure 1 summarizes the monthly mean emissions of six inventories for seven major biomass burning regions from April 2000 to March 2001. April 2000 is the time that MOPITT data became available. The seven regions represent source areas where the monthly average biomass burning emission can be characterized using monthly mean MOPITT CO columns and monthly mean GMD ground CO measurements [*Arellano et al.*, 2004; *Arellano*, 2005]. The global, annual biomass burning emissions (Table 2) vary by up to 28% relative to the mean annual emission of these six inventories (457 TgCO/a (where a is year)) with lowest from GFED2 (389TgCO/a) and highest from Arellano1 (518 TgCO/a).

[16] The seasonal peak in burning occurs around the same time for the different inventories over northern Africa (region 2), Central America (region 3) and Southeast Asia (region 5), but not in the other regions. There are two peaks over the NH boreal forest (regions 1) and southern Africa (region 6), as compared to one peak over other regions. For region 1, emissions peak in May 2000 and again in August 2000, except in GFED1 and Duncan2 which miss an emission peak in boreal spring and Duncan2 shows a second peak in July instead of August. GFED2 has the longest biomass burning emission season, starting in boreal spring and lasting into October. Both peaks in region 1 come from boreal forest with the latitude of the second further north. The wide coverage of region 1 is a shortcoming in our approach. In the future study, we should further divide this region to distinguish the biomass burning emissions from North America, Europe and Russia/northern Asia. For region 6, GFED2 peaks once in August 2000 instead of twice (i.e., June-July and September) as in the other inventories. Fire there usually starts over Congo in May and peaks during June and July (first peak) and then spreads and moves to eastern Africa (second peak).

[17] However, the most striking difference among these six inventories is their regional emission totals, which can vary by more than a factor of two. For instance, the two top-down emissions are about two to four times higher than the four bottom-up emissions over Central America (region 3)
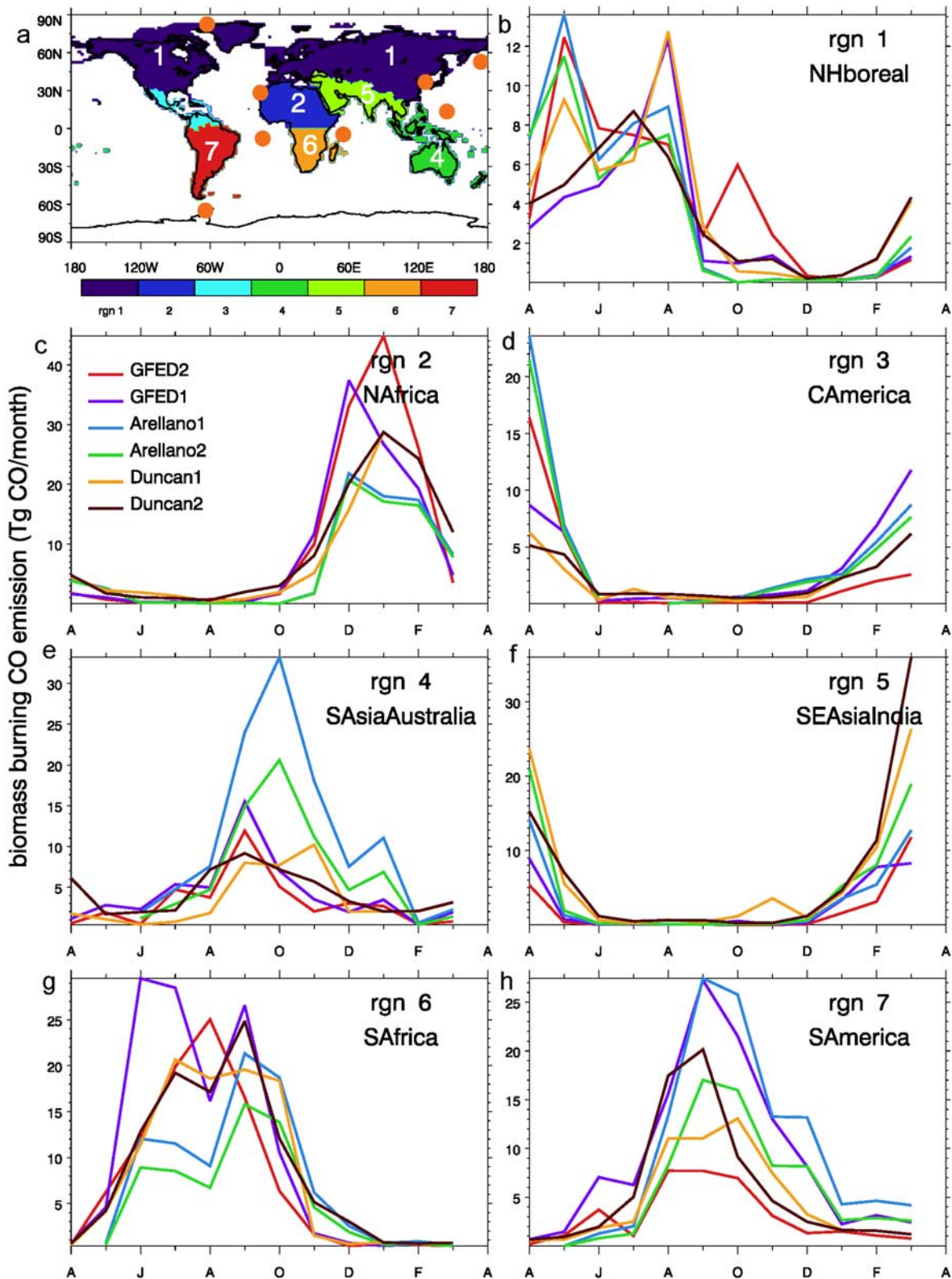
Figure 1. (a) Geographic distributions of seven biomass burning regional areas. The big orange dots are the location of GMD stations analyzed in Figure 2. (b–h) Monthly mean biomass burning emissions from six inventories on seven regions (region 1, middle to high Northern Hemisphere; 2, North Africa; 3, Central America; 4, Southeast Asia and Australia; 5, Southeast Asia, India, and Middle East; 6, southern Africa; 7, South America).

during April 2000. The highest monthly emission in South America is 27 TgCO for Arellano1 and GFED1 and 7 TgCO for GFED2. These significant discrepancies affect the simulated CO as discussed in the following subsections.

[18] The comparison of the climatological emissions of Duncan2 with the other year-specific emissions indicates that our study period had average biomass burning emissions. The deviation between the climatological and year-specific inventories usually does not exceed the variation among the year-specific emissions. One exceptional region is the NH boreal forest (region 1), where the climatological emission only has one peak in July, but many other emissions (GFED2, Arellano1, Arellano2, and Duncan1) have two peaks.

[19] The comparison of biomass burning inventories helps to identify strengths and weaknesses of inventories for regional modeling studies and highlights areas where emissions are highly uncertain. The importance of such study for the atmospheric science community drives a similar investigation conducted by *Hoelzemann* [2006]. The study examined five biomass burning inventories and their impact on tropospheric chemistry. The five biomass burning inventories given by *Hoelzemann* [2006] were the GWEM-1.3 inventory (GWEM) [*Hoelzemann et al.*, 2004], the inventory by *van der Werf et al.* [2003] (gfed), the climatological inventory of MOZART-2 developed by *Hao and Liu* [1994] (Hao&Liu), and two versions of the ATSR fire count scaled climatological inventories: *Schultz* [2002] (mgs_scal) and Granier and Lamarque [*Hoelzemann*, 2006] (cg_scal). The global biomass burning CO emissions used by *Hoelzemann* [2006] lies between 30 and 38% of the total CO emission. These percentages of biomass burning contributions are close to the range of 28–38% in our study (Table 2). There is one overlap in biomass burning emission inventory use in the study by *Hoelzemann* [2006] and our study: both studies make use of the GFED1 emissions, which show very low emissions during NH spring and have a distinct peak in September in South America as a result of elevated deforestation fire emissions (*Hoelzemann* [2006, Figure 3.3] and Figure 1, regions 1 and 7, in this work).

2.1.2. Fossil Fuel and Biofuels

[20] Atmospheric CO is released directly from fossil fuels, biofuels, and biomass burning. The base CO inventory used in this study is described by *Bey et al.* [2001] for fossil fuel and *Yevich and Logan* [2003] for biofuels. These emissions are compiled on an annual mean basis for the TRACE-P studies. The base inventory in Asia in the year 2000 for both fossil fuel and biofuels is compiled by *Streets et al.* [2003] by summarizing statistical environment and energy data. However, we increase the Asian fossil fuel emissions by 46% (39% direct emission and 7% the secondary source), on the basis of new findings of enhanced anthropogenic emissions estimated by *Streets et al.* [2003] from forward and inverse CTM studies [*Palmer et al.*, 2003; *Heald et al.*, 2003; *Allen et al.*, 2004; *Arellano et al.*, 2004; *Tan et al.*, 2004; *Wang et al.*, 2004]. Our emission enhancement is close to the new estimation by *Streets et al.* [2006] that is 36% higher, reflecting additional sources which were missed in the 2000 inventory.

2.1.3. Photochemical Production of CO in the Model

[21] CO is also produced by photochemical reactions from NMHC and CH_4. Production of CO from anthropogenic and biomass burning NMHC is derived by multiplying the emission rate of each NMHC in a given inventory and a yield of CO per carbon atom oxidized with yields taken from *Altshuller* [1991]. Applying these yields, we find that oxidation of NMHC results in a source of CO that amounts to about 20%, 19% and 11% of the direct emissions of CO from fossil fuels, biofuels, and biomass burning, respectively. The emissions of CO from these three source categories are increased by these amounts to account for the secondary CO source from oxidation of the coemitted NMHC.

[22] For CO from biogenic NMHC, we adopted the NMHC emissions calculated from the Global Modeling Initiative (GMI) CTM, which uses the same meteorological fields as the simulations presented here. The distribution of biogenic isoprene is based on a modified version of the inventory of *Guenther et al.* [1995], and is dependent on solar radiation and temperature. The principal modifications are a decrease in the leaf area index (LAI) from tropical forests and an improved representation of light attenuation within the forest canopy as described by *Wang et al.* [1998], and a reduction in emission rates for several ecosystems so that simulated and observed isoprene concentrations agree better [*Bey et al.*, 2001]. The distribution of monoterpene emissions is also taken from *Guenther et al.* [1995] as modified by *Wang et al.* [1998]. A biogenic methanol source of 37 Tg C [*Singh et al.*, 2000] is distributed according to emissions of isoprene with a yield of 1 CO from methanol oxidation. The primary acetone emissions from biogenic sources are about 16TgC/a [*Jacob et al.*, 2002] and the yield of CO from the oxidation of acetone is about 0.66 on the basis of degradation pathways given by *Orlando et al.* [2000]. The CO from acetone is much lower compared to other sources and thus is neglected in our study. We assume a CO yield of 0.2 from the oxidation of isoprene [*Miyoshi et al.*, 1994], terpene [*Hatakeyama et al.*, 1991; *Vinckier et al.*, 1998], and other NMHCs. The CO from these sources is treated as direct emission from the surface, assuming rapid NMHC oxidation.

[23] Methane oxidation is a major source of CO. The monthly CH_4 fields used in this study are compiled from the long-term GMD GLOBELVIEW-CH_4 observations (http://www.cmdl.noaa.gov/ccgg/globalview/index.html) and are a function of latitude. A range of 0.78 to 1.0 of CO yield from CH_4 oxidation are reported by previous studies [*Logan et al.*, 1981; *Tie et al.*, 1992; *Manning et al.*, 1997; *Novelli et al.*, 1999; *Bergamaschi et al.*, 2000; *Arellano et al.*, 2004], though more recent estimates are closer to 1 [*Duncan et al.*, 2007]. We adopt a yield of 1 for this study.

[24] The main sink for CO is its reaction with OH. We use monthly mean OH fields which are from a combination of tropospheric fields of the year 2001 from the GEOS-CHEM tropospheric chemistry model [*Bey et al.*, 2001; *Park et al.*, 2004] and stratospheric fields of the year 1995 from the GMI model [*Kinnison et al.*, 2001]. The global mean OH of this work is 9.96e05 molecules/cm^3, which is similar to 9.7e05 molecules/cm^3 from *Prinn et al.* [2001] and 11.6e05 molecules/cm^3 from *Spivakovsky et al.* [2000]. The global lifetime of CH_3CCl_3 with respect to tropospheric OH is 5.6 a for this work and it is slightly shorter than 6.0 (+0.95, −0.7) a from *Prinn et al.* [2001] and 5.9 a from *Spivakovsky et al.* [2000].

Table 3. Statistical Analyses for the Percent Differences Between Simulated and Observed Surface CO[a]

	Maximum Percent Difference		Annual Mean Percent Difference	
	Range	Mean	Range	Mean
Europe-Asia inland and Asia coast region	12−25%	17.1%	4−6%	5.1%
Other NH mid-high latitudes	6−12%	9.0%	4−7%	4.9%
NH subtropical region	6−15%	10.3%	4−7%	5.4%
Tropical and SH subtropical regions	20−44%	27.3%	8−18%	11.3%
SH mid-high latitudes	17−22%	19.1%	12−13%	12.4%

[a]Model simulations use six biomass burning inventories in Tables 1 and 2. The observations are obtained from all GMD ground stations. GMD station (http://www.cmdl.noaa.gov/ccgg) groups: Europe-Asia inland and Asia coast region (including stations of HUN, BSC, KZD, UUM, TAP); other NH middle to high latitudes (ALT, ZEP, STM, ICE, BRW, CBA, SHM, MHD, AZR, BAL, WLG, UTA, NWR, LEF, BME, BMW); NH subtropical region (IZO, WIS, MID, MLO, GMI, KUM, RPB); tropical and SH subtropical regions (CHR, ASC, SEY, SMO, EIC); and SH middle to high latitudes (TDF, CRZ, PSA, SPO, HBA, SYO). See also Figure 2.

2.2. Observational Data

[25] We use observations of CO from three sources to evaluate our simulations. First, the NOAA Global Monitoring Division (GMD) Carbon Cycle Greenhouse Gases (CCGG) observational network (http://www.cmdl.noaa.gov/ccgg/index.html) provide long-term station measurements. Sampling frequencies are approximately weekly at local noon for surface fixed sites and usually one to two times per month in local afternoon for aircraft measurement over aircraft sampling sites. Flagged data are excluded from our comparisons.

[26] Second, the NASA Transport and Chemical Evolution over the Pacific (TRACE-P) field campaign took place over the northwest Pacific during February-April 2001 [*Jacob et al.*, 2003]. CO was measured with a 1 s sampling frequency using differential absorption spectrometry [*Sachse et al.*, 1987] with an accuracy of approximately 2% [*Heald et al.*, 2003]. We use 1-min merges prepared by L. Emmons (private communication, 2005) for all DC-8 and P-3B measurements.

[27] Third, CO data retrieved from the Measurements Of Pollution In The Troposphere (MOPITT) instrument on the EOS-Terra satellite is available since April 2000. The retrieval averaging kernels, which are a linear representation of the vertical weighting of retrievals, are dependent on the surface albedo, the surface to air temperature contrast, an a priori CO vertical profile, and a covariance matrix of the uncertainty in the a priori CO profile [*Lamarque et al.*, 2004]. The retrieval algorithm adopts a methodology which seeks the solution that is the most statistically consistent with both the measured radiances and the typical observed patterns of CO profile variability [*Pan et al.*, 1998; *Deeter et al.*, 2003]. MOPITT's orbit has an equator crossing time of 1045 local time (LT) and its cross-track scanning allows for near global coverage in 3 d. We use level 2 version 3 column CO products with 22 km horizontal resolution and roughly 10% precision [*Deeter et al.*, 2003; *Emmons et al.*, 2004]. The retrieved column data is most sensitive to the middle troposphere and least to the surface [*Deeter et al.*, 2003]. Validations for MOPITT retrieval have been conducted by various regular aircraft measurement sites and a number of campaigns [*Emmons et al.*, 2004]. The validation indicates that the biases of retrievals are 8−10 ppbv in the lower troposphere, 2−5 ppbv in the midtroposphere, and a slight negative value in the upper troposphere and lower strato-sphere over evaluation sites. We calculate the model CO column using the same averaging kernel used in the MOPITT retrieval.

3. Simulated CO in Response to Biomass Burning Emissions

3.1. Surface Concentrations

[28] A statistical analysis of measurement and model surface CO comparisons is given in Table 3. Six model CO results are used in the comparison with each corresponding to an emission shown in Table 2. The analysis is performed over 39 GMD surface stations for an overall model performance. We group the GMD surface stations into 5 groups (Table 3). The geographical locations of these GMD stations are shown on Figure 2. We characterize the variation of model CO due to different emission inventories by using two parameters, maximum CO percent difference (MPD) and annual mean CO percent difference (AMPD). At each station, we first calculate the CO percent difference between model and observation for each month. The MPD is then defined as the maximum value of the calculated monthly difference during the year and the AMPD is defined as annual mean of the difference. The MPD reveals how large the perturbation of the CO fields can be due to different biomass burning inventories, relative to the observed, while the AMPD, by comparing with MPD, exhibits how long this perturbation persists. It is notable that although MPD itself represents an overall influence of more than just biomass burning, the variations of MPD over different regions can provide such information when the regions are impacted by burning emissions at different extents.

[29] Statistically, CO in the Southern Hemisphere (SH) is more sensitive to biomass burning inventories than in the Northern Hemisphere (NH). The CO MPD is 17−22% with a mean of 19.1% in the middle to high-latitude SH, compared with a range of 6−12% and mean of 9.0% in the NH background environment. This is because the fraction of total CO contributed from biomass burning is much smaller in the NH than in the SH (see Figure 3 below). Stations in the interior of the Europe-Asia continents and the Asian coast regions are special in that they show almost double the MPD compared with other NH middle to high-latitude stations, although the AMPDs of the
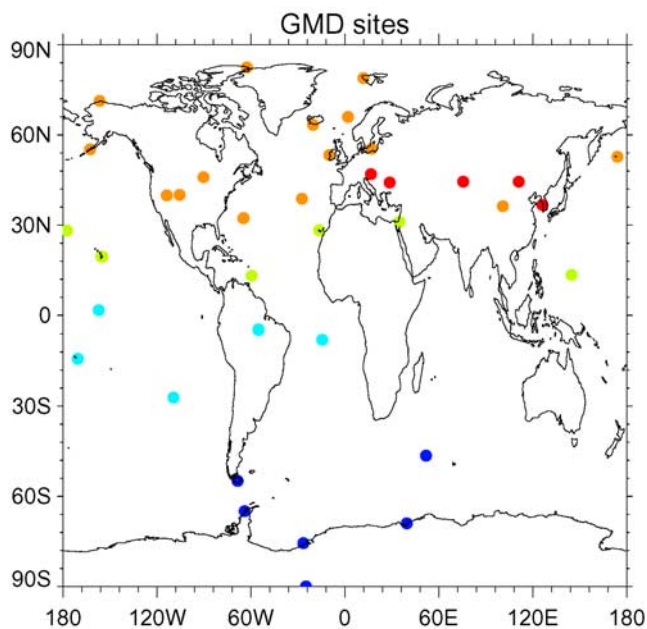
Figure 2. Geographical locations of GMD stations used in Table 3. Each color represents one station group: Europe-Asia inland and Asia coast region (red); other NH middle to high latitude (orange); NH subtropical region (olive green); tropical and SH subtropical regions (light blue); and SH middle to high latitudes (dark blue).

two groups do not differ much. Globally, the tropical and SH subtropical regions have the highest MPD because they are closer to the biomass burning emission regions and because the biomass burning CO constitutes a large fraction of total CO there. However, AMPD shows a consistent latitude gradient with highest values in the high-latitude SH (average as 12.4%) and lowest in the high-latitude NH (average 4.9%).

[30] Does difference in biomass burning emissions matter in modeled CO? Our analyses indicate that it does matter in the regions strongly influenced by biomass burning sources, for example, the MPD reaches 44% at ASC. Since the GMD network is designed for monitoring the atmospheric back-ground environment, it is more appropriate to use GMD sites to assess the mean influence on calculated CO. The background surface CO variation from different biomass burning inventories in the SH shows AMPD > 12%. The surface CO in the NH background atmosphere is not as sensitive to the alternative biomass burning emissions (AMPD< 5%) although the regional emission variation in the NH is substantial (Figure 1).

[31] The model-observation comparisons at 8 selected GMD surface stations are shown in Figure 3 for further examination. The stations are selected to represent different biomass burning and ocean regions shown in Figure 1. Along with the modeled CO simulated by different biomass burning inventories, the modeled CO without biomass burning emission is also shown on Figure 3 to illustrate the fraction of total CO contributed by biomass burning emission at different geographic locations. The model captures both the magnitude of seasonal variations and the mean CO mixing ratio at most locations, except at a SH

high-latitude station (Palmer Station, Antarctica, PSA), where simulated CO is 10–25% higher than observation. There are several possibilities for this overestimated CO, such as emissions or photochemical production are too high and loss to OH oxidation is too low in the SH; or interhemispheric transport is too strong. Figure 3 also confirms that biomass burning CO constitutes a much smaller fraction of total CO in the NH than in the SH.

[32] All the differences between CO in Figure 3 reflect the different biomass burning emissions in Figure 1. NH stations, Tae-ahn Peninsula (TAP), Shemya Island (SHM), and Alert (ALT), have higher simulated CO from GFED2 during boreal fall season, consistent with much higher biomass burning emissions from GFED2 in October for region 1 (Figure 1). Interestingly, the CO response period at these three stations is slightly different from middle to high latitudes, ranging from October for TAP, October to November for SHM, and November to December for ALT. We analyzed all GMD stations in the NH middle to high latitudes and found that this delayed 1–2 months of the response in surface CO depends generally on latitude but not on longitude. This indicates that the atmosphere takes 1–2 months to transport CO from NH middle to high latitudes during boreal fall season. However, the transport time may vary in subject to the seasons. For example, *Lamarque and Hess* [2003] analyzed the age distribution of European emissions over high latitudes (60°–90°). The study found that the majority of January CO over high latitudes came from January CO in the source region, while the maximum contribution of May CO is released during April in Europe.

[33] Northern tropical station Tenerife, Canary Islands (IZO) is located at a high-elevation mountain site close to northern Africa. A NH tropical Atlantic gyre brings marine air over this station during boreal winter season. Therefore CO at IZO generally represents atmospheric background levels so that biomass burning in northern Africa winter season shows little impact at IZO. Another northern tropical station Guam, Mariana Islands (GMI) is impacted by biomass burning emissions from Southeast Asia in spring, where GFED2 and GFED1 give about 57% and 40% lower emission than the mean emission in April (Figure 1). Correspondingly, the surface CO at GMI in April for GFED2 and GFED1 is around 7.9% and 5.7% lower than average. Although there is about 15% variation in simulated CO at GMI using different biomass burning inventories, the model CO results are still within the range of the observed CO variation.

[34] CO at SH stations (i.e., Seychelles, Mahe Island (SEY), Ascension Island (ASC), and Palmer Station, Antarctica (PSA)) is more sensitive to the uncertainty of the biomass burning emissions, which confirms our discussion for Table 3. For example, the MPD reaches 44% at station ASC during the biomass burning season over southern Africa where the emissions from the six inventories vary by as much as a factor of 4. The range of modeled CO values once again fall within the observed CO range over ASC since the variation of measured CO is also very large during the biomass burning season. Furthermore, unlike the NH stations, CO at SH stations is impacted for a longer period (Figure 3). The range of model CO over middle and high SH, e.g., PSA, is typically around 8 ppb in all seasons
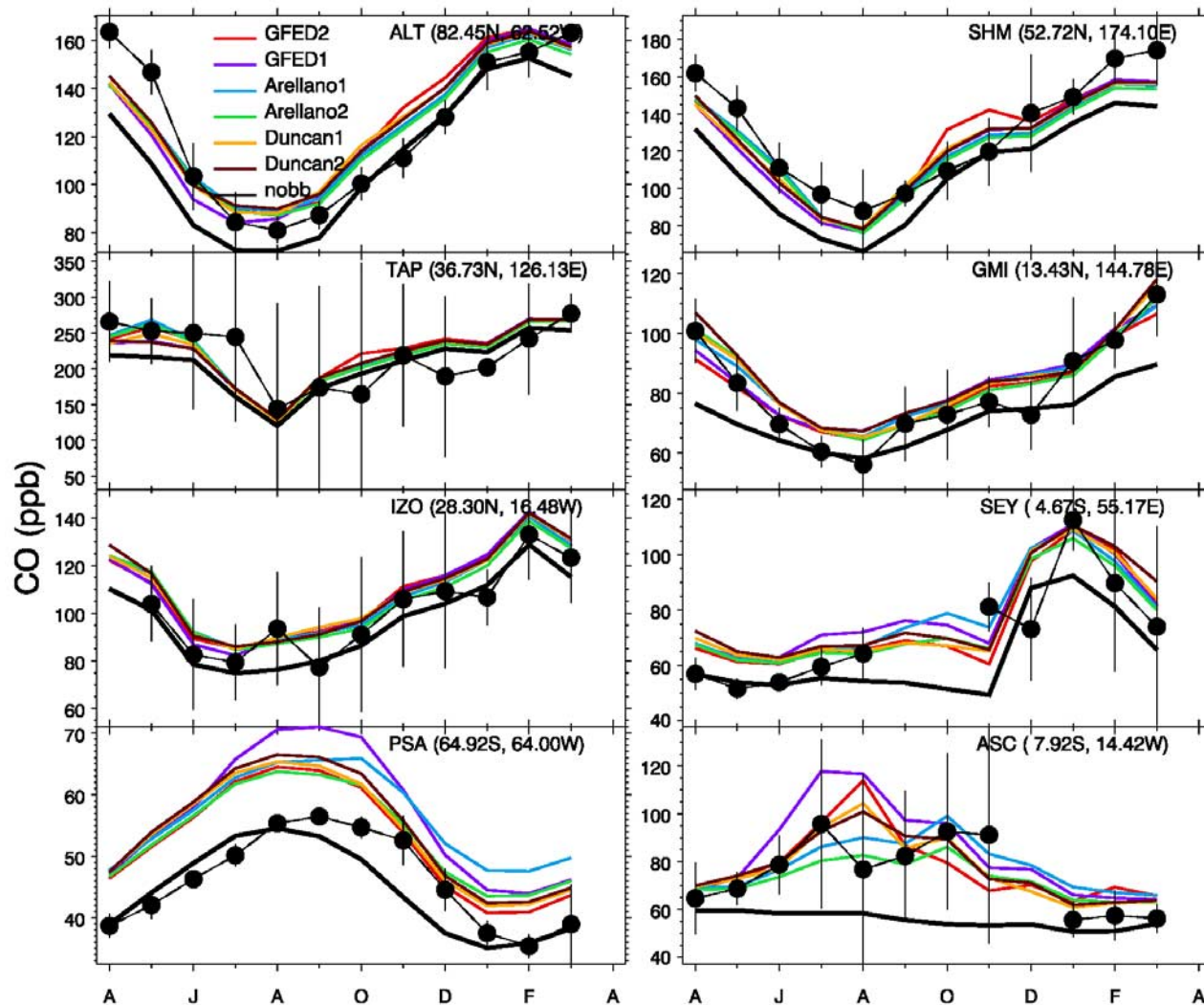
Figure 3. Surface CO mixing ratios (ppb) at GMD stations. Solid line with dots stands for CO monthly mean from GMD measurements; solid color lines are from model simulations using different biomass burning emissions as indicated in the legend, and solid thick black line is model CO without biomass burning.

except during austral fall. The sum of biomass burning emissions from the SH regions (i.e., Australia, southern Africa, and South America) are 161 (GFED2), 277 (GFED1), 305 (Arellano1), 199 (Arellano2), 193 (Duncan1), and 218 (Duncan2) TgCO. The highest emission from Arellano1 (35% higher than average) and the lowest from GFED2 (29% lower than average) explain the simulated highest and lowest CO concentrations over PSA. There is a clear bias in the model at certain times (e.g., PSA from January to October and ALT in boreal spring and fall) which is larger than the differences induced by different biomass burning emissions. This systematic error may be related to hemispheric transport issues or to low OH abundances of GEOS-CHEM over Southern Hemispheric high latitudes. OH observations from ISCAT 2000 reported higher OH in the high-latitude Southern Hemisphere [*Mauldin et al.*, 2004].

3.2. Column Burden

[35] Column CO from MOPITT and from model simulations are shown in Figure 4 for April and Figure 5 for October. These months are chosen to depict the most significant differences among the various biomass burning source simulations [*Shindell et al.*, 2006]. Figures 4 and 5 also include the model CO without biomass burning emission to illustrate where and when burning has a large contribution to atmospheric CO. All intensified local column CO shown in Figures 4 and 5 is associated with fires. For example, April is a month in the burning season of Southeast Asia. The peak biomass burning emission over South America occurs in October. Africa undergoes burning over a long period of time. In January (not shown), large fires occur in NH Africa near the Gulf of Guinea. The burning moves southward in boreal summer and continues toward southeast Africa in boreal fall (Figure 5).

[36] Globally, the simulated distributions capture the main features revealed by satellite observations from the
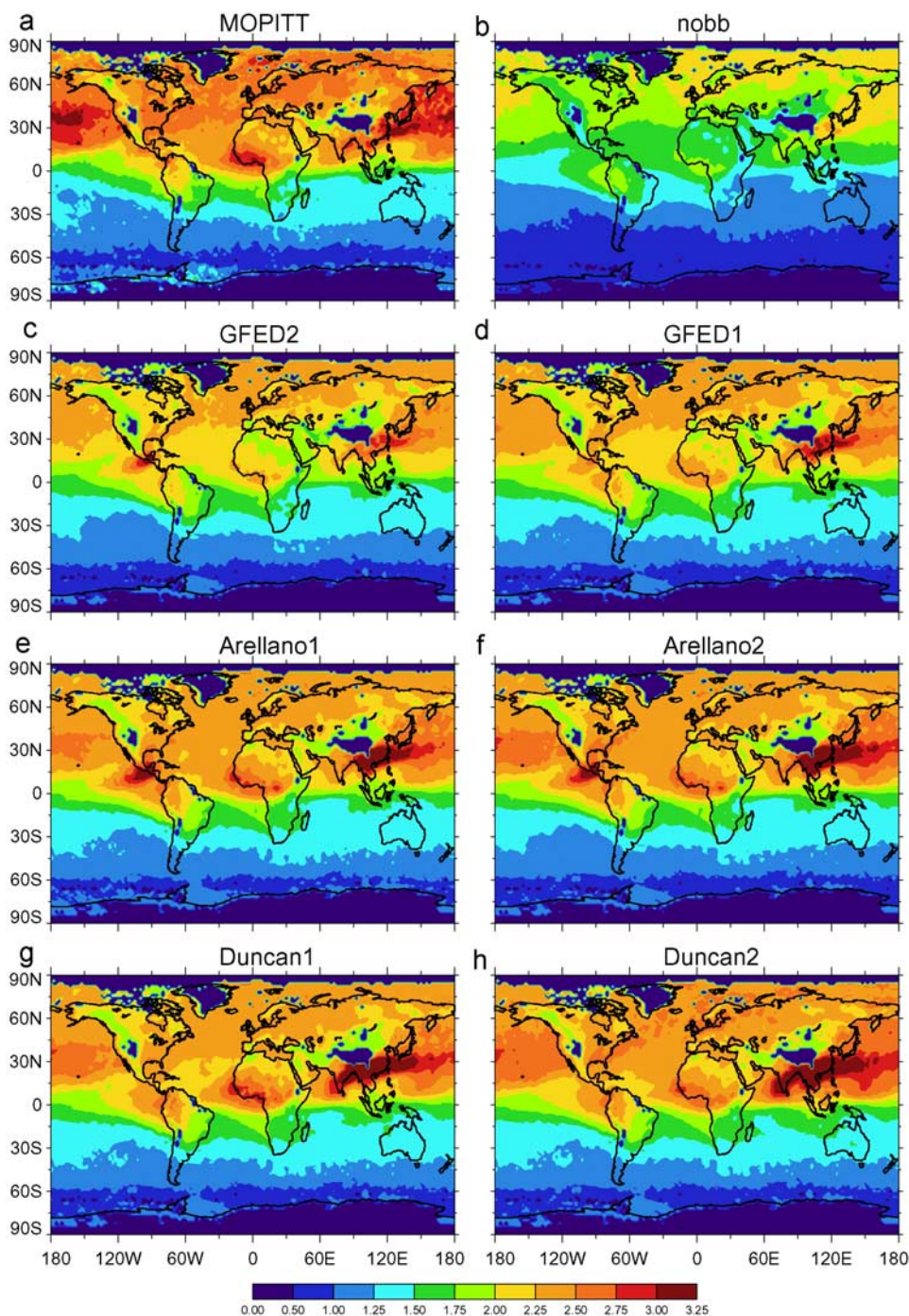
Figure 4. Global column CO (10^{18} molecules/cm^2) distributions in April 2000 from (a) MOPITT observation, (b) model simulation without biomass burning, and (c–h) model simulation with six burning inventories. Model CO columns have been converted using the same averaging kernel used in MOPITT retrieval in order to compare with MOPITT observation.

MOPITT instrument, for example, the interhemisphere gradient, the CO maximum over Southeast Asia and downwind over the north Pacific Ocean (biomass burning) and industrial regions (fossil fuel and biofuel). Some fine features of the comparison are caused by topography, such as Greenland and high mountains. In areas of elevated topography, where one or more of the fixed pressure level values in MOPITT retrieve exceed the actual local surface

pressure, the retrieved state vector is filled with the missing value numerical identifier (http://mopitt.eos.ucar.edu/mopitt/data/index.html). Others may be induced by persistent clouds which obviate the retrieval. It is also interesting to note that no biomass burning inventory leads to the high values seen over the Pacific and Atlantic oceans.

[37] There are similarities in biomass burning CO from emissions constructed with the same source data and
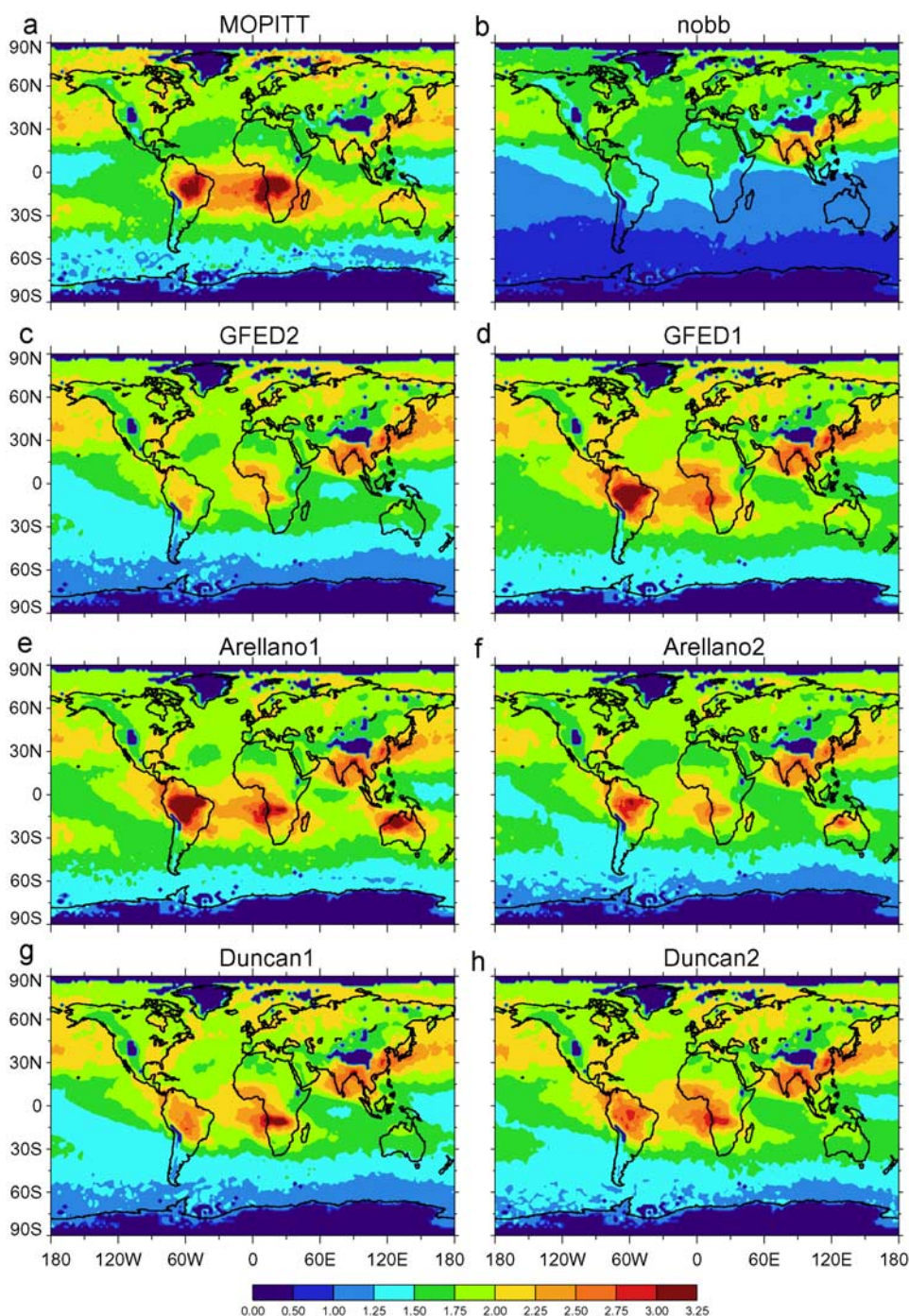
Figure 5. Same as Figure 4 but for October 2000.

techniques. For example, the column CO distributions from TOMS-based emissions, Duncan1 and 2, look more similar to each other with high CO over both Southeast Asia and India in April, while TRMM-based emissions GFED1 and 2 produce less CO over India (Figure 4). Furthermore, TRMM-based emissions Arellano1 and 2 give a similar high CO over Central America in April.

[38] One motivation for this work is to determine an optimal choice of biomass burning emission from the various current available inventories. Figures 4 and 5 provide useful information for such analyses. However,

caution should be taken to recommend biomass burning inventory on the basis of the comparison of column CO between model and MOPITT. This is because the difference is not only caused by bias in biomass burning, but also induced by uncertainties in other emissions, chemistry, and transport processes. Fortunately, for tropical regions, the evaluation can be relatively straightforward on the basis of model-MOPITT comparison by contrasting the data between biomass burning and nonburning seasons. In tropical regions, biomass burning CO during fire season exceeds CO from all the other sources and processes, as

manifested in Figures 4 and 5. The overall amplitude of the CO seasonal cycle stemming exclusively from fires is much higher than the amplitude of CO from a simulation without biomass burning. Sometimes seasonal variation induced by biomass burning emission can be of the same order as the discrepancies resulting from the use of different inventories (Figures 4 and 5). In addition, model CO can have a substantial difference from MOPITT CO on regional scales and the large difference usually occurs in regions where biomass burning is large. Figures 4 and 5 indicate that each biomass burning inventory provides a good agreement between the model results and observations for some regions and seasons, but not others.

[39] It is difficult to judge biomass burning emission over NH Southeast Asia where most CO emissions come from fossil fuel and biofuel (FFBF) even during local biomass burning season (Figure 4). However, the importance of FFBF and biomass burning to atmospheric CO varies with altitude. A field campaign, TRACE-P, was conducted in this region in the spring of 2001. The model-aircraft comparison will be introduced in the next section to discern a systematic FFBF error embedded in six model results and help us to identify an optimal biomass burning inventory in this region.

[40] Over Southeast Asia, intensified burning activities occur during boreal spring season (see Figure 1, region 5, and Figure 4). The model CO over Southeast Asia in April varies significantly with different burning emissions. The modeled CO is higher than MOPITT CO over Southeast Asia and the adjacent area of the northwest Pacific from TOMS-based emissions (Duncan 1 and 2) and from two TRMM-based top-down emissions (Arellano 1 and 2). Such discrepancy was also reported by a number of TRACE-P studies for March 2001 [*Heald et al.*, 2003; *Palmer et al.*, 2003; *Allen et al.*, 2004; *Wang et al.*, 2004], where the biomass burning emissions used were the same or similar to the inventories of *Duncan et al.* [2003]. By comparing with TRACE-P aircraft measurements, these studies concluded that biomass burning emission from Southeast Asia is overestimated by 40–70%. GFED2 gives a lower CO column than MOPITT but GFED1 produces a distribution similar to MOPITT. However, as we discussed above, caution should be taken here in recommending biomass burning emission because of a large CO emission from industrial and domestic wood fuel use in Asia. We will revisit emission inventories in Southeast Asia with an evaluation using aircraft measurements in the next section. On the other hand, CO in all model simulations is lower than MOPITT CO over the central Pacific in this period, similar to what was shown in previous studies [e.g., *Heald et al.*, 2003, Figure 3; *Arellano et al.*, 2006, Figure 6] but no reason was given. We need to investigate whether there is cloud contamination in MOPITT retrieval during this period in this location, whether the injection height of burning adopted in the model is too low, or whether the model convection over Southeast Asia is not strong enough.

[41] Over Central America, where biomass burning also occurs in boreal spring season, model CO is too high for inventories of Arellano1, Arellano2, and GFED2 compared to MOPITT (Figure 4). The two top-down emissions release almost triple the CO of GFED1 (region 3 in Figure 1). The anomalous high-column CO simulated using Arellano 1 and

2 and GFED2 exceeds the uncertainty range that could be inferred from other processes. The emissions from GFED1 and from Duncan 1 and 2 give more reasonable CO simulations in this region. The anomalous column CO in Central America suggests that more investigation of the inverse work is required.

[42] Biomass burning over South America dominates the local atmospheric CO during October (Figure 5) and the six emission sets vary substantially (Figure 1, region 7). Without biomass burning emissions, the maximum column CO is about 1.50×10^{18} molecules/cm^2. With biomass burning emissions, column CO ranges from 2.25×10^{18} using GFED2 to 3.97×10^{18} using Arellano1. Compared with MOPITT data, CO from GFED2, Arellano2, Duncan1 and 2 are too low, while CO from Arellano1 and GFED1 are too high. GFED1, however, was reported to be favored among the five biomass burning emissions studied by *Hoelzemann* [2006] for South America. In addition, CO simulated with GFED2 is lowest over South America, reflecting the lowest emission amount in GFED2. The underestimation of South America's emission in GFED2 is attributed to cloud cover and other limitations, as reported in the GFED2 description [*van der Werf et al.*, 2006].

[43] Fires have an important share on CO concentrations over the African continent [*Hoelzemann*, 2006]. A high CO regime from western Africa to the tropical Atlantic in January results from NH Africa biomass burning fire (Figure 1). This NH Africa fire is very intensive, but the variation of model CO due to six inventories is not as large as the variations of other fires. Therefore the strong NH Africa fire is easier to identify and is represented relatively well in all inventories based on model-MOPITT comparison. There are significantly differences in six biomass burning emissions in SH Africa in May to July (Figure 1). None of the inventories represents the burning season well in this region (not shown). Emissions from GFED1, 2 and Duncan1, 2 are too high, while emissions from Arellano1 and 2 are too low. Another peak of burning over SH Africa occurs during September to October (Figure 5). Model CO amounts from all biomass burning emissions are considerably underestimated compared with MOPITT, which is also concluded by *Hoelzemann* [2006].

[44] Statistical analyses (Table 4) are applied to quantitatively assess the quality of simulations by using mean bias, which represents the ratio of the model column amounts to the data, and the linear correlation coefficient. The annual mean parameters are calculated using the average value of four monthly means (April, July, October, and January).

[45] Globally, the difference in column CO distributions given by different biomass burning emissions (shown in the last column in Table 4) is 5% for bias and 3% for correlation. It is reasonable that the top-down emission derived from the MOPITT measurements gives the highest correlation. It is also understandable that, among six results, global annual CO is lowest from GFED2 and highest from Arellano1 by considering their emissions in Table 2.

[46] Regionally, the variation in the SH is generally larger than in the NH. The difference is around 10–13% in the SH regions and 2–7% in the NH regions. This column CO difference due to different biomass burning inventories, therefore, has a similar magnitude to the variation of surface CO discussed above. An overall performance of burning

Table 4. Statistical Parameters for the Comparison of Global and Regional Annual Mean CO Between Model and MOPITT Satellite Data[a]

	GFED2	GFED1	Arellano1	Arellano2	Duncan1	Duncan2	Max-Min
				Bias			
Global	0.96	1.01	1.01	0.97	0.98	**1.00**	0.05
reg1, NHboreal	0.96	0.96	0.97	0.96	0.97	**0.98**	0.02
reg2, NAfrica	0.98	1.01	0.98	0.95	**1.00**	1.02	0.07
reg3, CAmerica	**1.02**	1.09	1.08	1.04	1.05	1.07	0.07
reg4, SAsiaAustralia	0.92	**0.99**	1.05	0.97	0.94	0.98	0.13
reg5, SEAsiaIndia	**1.00**	1.03	1.03	1.02	1.05	1.07	0.07
reg6, SAfrica	0.94	**0.99**	0.94	0.89	0.95	0.95	0.05
reg7, SAmerica	0.96	1.08	1.07	0.99	**1.00**	1.02	0.12
NHO	0.97	0.98	0.98	0.97	0.98	**1.00**	0.03
TPO	0.97	1.03	1.03	0.99	**1.00**	1.02	0.05
SHO	0.93	**1.02**	1.03	0.96	0.95	0.97	0.10
				Correlation			
Global	0.90	0.90	**0.93**	0.92	0.91	0.91	0.03

[a]The global and regional least bias and global best correlation from six inventories are in bold.

emissions shown in Table 4 over a certain region, however, may not be consistent with the results shown in Figures 4 and 5. Take Central America (CA) for example. The burning season there occurs in April (Figure 1) and the simulated CO concentrations using GFED2 are much higher than MOPITT retrieve in that month (Figure 4). On the annual basis, however, GFED2 gives the best result over CA (Table 4). This is because simulated CO concentrations over CA are strongly impacted by South America (SA) outflow because they border each other. GFED2 has been identified to be too low in SA (see our discussion above; also see Figure 5 for October when SA is in burning season). Therefore the smallest regional bias over CA on an annual basis (Table 4) is a compromised result of the high local but low surrounding burnings.

[47] Figure 6 displays probability distributions of column CO from MOPITT (thick black line) and six model data (thin color lines) over the regions shown in Table 4. A burning month is picked for each region in Figure 6 to highlight the burning influence. The PDF patterns of MOPITT and models are similar to each other except in the NH boreal region (region 1) where the model column CO is consistently lower than MOPITT. This indicates that some processes other than biomass burning are not well represented by the model in this region or all inventories underestimate the emissions. The differences due to different biomass burning emissions are usually manifested at the high end of the CO amounts, and are consistent with high CO values shown on Figures 4 and 5. For example, the significant variation of atmospheric CO over the South America burning season (Figure 5) is shown in Figure 6, region 7. The PDF for GFED2 is negligible at column CO greater than 2.5×10^{18} molecules/cm^2, where MOPITT and other models still have significant probability. This indicates that GFED2 underestimates burning emission over South America substantially. The burning area and strength of Duncan1 and 2 and Arellano2 are also lower than MOPITT, but Arellano1 and GFED1 are higher. These features reinforce the conclusions we got from analyzing spatial column CO distributions in Figure 5.

3.3. Vertical Profiles

[48] The vertical distributions of the modeled CO are compared with GMD aircraft measurements in Figure 7 at station Santarem, Brazil (SAN: 2.85°S, 54.95°W). Aircraft measurements were conducted on 7 and 21 December, both in the afternoon. The measurements indicate a significantly different CO vertical distribution between these 2 d. It appears that local emissions were greater on 7 December as CO mixing ratios were higher through a deeper boundary layer. December atmospheric CO at SAN is dominated by biomass burning emissions from South America; however, emission from western Africa may also affect CO in SAN via long-range transport. Our simulations illustrate that CO is very sensitive to the biomass burning inventories at this site. The differences among the simulated CO concentrations from different biomass burning inventories on 7 December can be twice those of 21 December. The TRMM-based bottom-up and top-down emissions (GFED1, Arellano1, and Arellano2) give larger CO values than those of TOMS-based emissions (Duncan1 and Duncan2). However, the new version of TRMM-based emission (GFED2) results in CO distributions that are more similar to TOMS-based emissions. The order of simulated CO magnitudes (Figure 7) is consistent with the order of the emission amounts shown in Figure 1 in South America (region 7). A distinct boundary layer structure observed on 7 December is not captured by model simulations, which indicates that the model's vertical transport may need to be improved. Also note that the monthly mean biomass burning emissions used in the model simulation will not capture day-to-day variations likely influencing the observations. This inadequate model representation highlights the importance of matching temporal scales of emissions for detailed model-observation comparisons. It may also suggest a need in CTMs to inject fire emission plumes well above the surface as indicated by *Freitas et al.* [2006].

[49] Table 5 summarizes the mean biases between modeled and measured CO over the 37 TRACE-P flights. Two NASA aircrafts, DC8 and P-3B, were used during spring 2001. Our model-measurement comparisons indicate a possible systematic difference between the measurements of the DC8 and P-3B. DC8 gives about 5% higher CO mixing ratio than P-3B measurement over coast region,
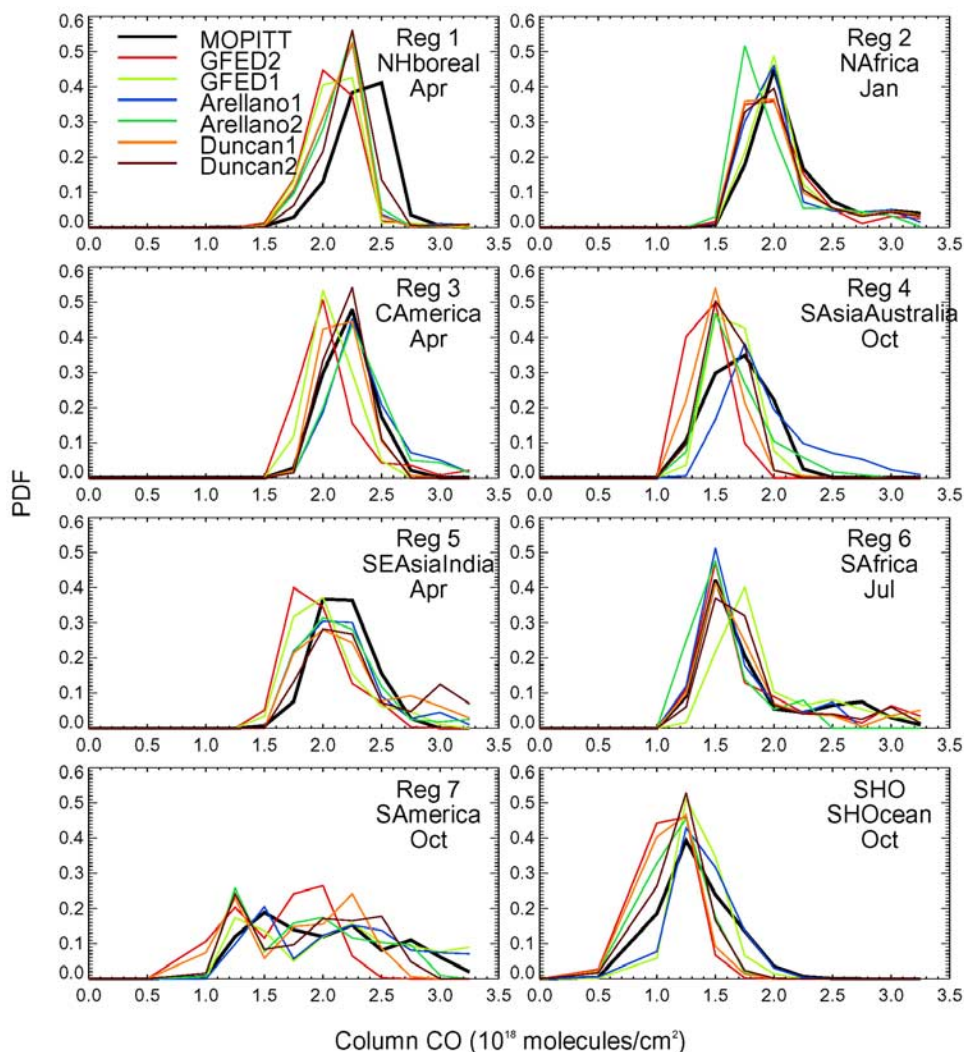
Figure 6. PDF of column CO over seven land regions (Figure 1) and over SH ocean. Burning month is picked for each region.

while CO measured from DC8 is lower than P-3B by about 2% over Central Pacific. Different sampling could be a potential reason for the difference. We feel further investigation is needed to examine this systematic difference. Generally, model CO is closer to observed CO over the coastal region than over the remote Pacific. The variation of the six emissions is around 10–13% over the coast region and 7–10% over the remote region. GFED2 once again gives the lowest CO and Duncan2 gives the highest. Nevertheless, it is hard to recommend a particular emission on the basis of Table 5 since the comparison is also affected by uncertainty in other factors, such as emissions from industry.

[50] Typical model vertical profiles are compared with aircraft measurements conducted in TRACE-P (Figure 8). Also shown in Figure 8 are their corresponding flight tracks with three measurements over western Pacific and two trans-Pacific measurements. These five flights are selected from a total of 37 flights in terms of their geographic representation, and especially their CO vertical distributions. Simulations generally capture measured CO vertical structures. Three measurements over the East China Sea show CO outflow from east Asia to the Pacific, although the altitude of the outflow layer for each case is different. The boundary CO outflow should mostly come from the local sources in east China, which composes most of the industrial emission. This is evident on Figure 8 where CO concentrations simulated using different biomass burning emissions are almost the same within PBL. On the other hand, whenever there is outflow at high altitudes, CO concentrations simulated by different inventories show more divergence, which illustrates that biomass burning emission over Asia does play a role at higher altitudes. This pattern is also reflected in vertical ozone profiles influenced by biomass burning emissions over this area in the study of *Hoelzemann* [2006, Figure 4.38]. CO simulated by the two TOMS-based bottom-up emissions in March are too high in the outflow above the PBL, but not inside PBL, indicating that TOMS-based emissions are overestimated. *Allen et al.* [2004] used the same biomass burning emission as Duncan2 for the flight of 13 March and reached the same conclusion.

[51] Vertical variation of CO measured by two trans-Pacific flights is relatively small compared to the variation
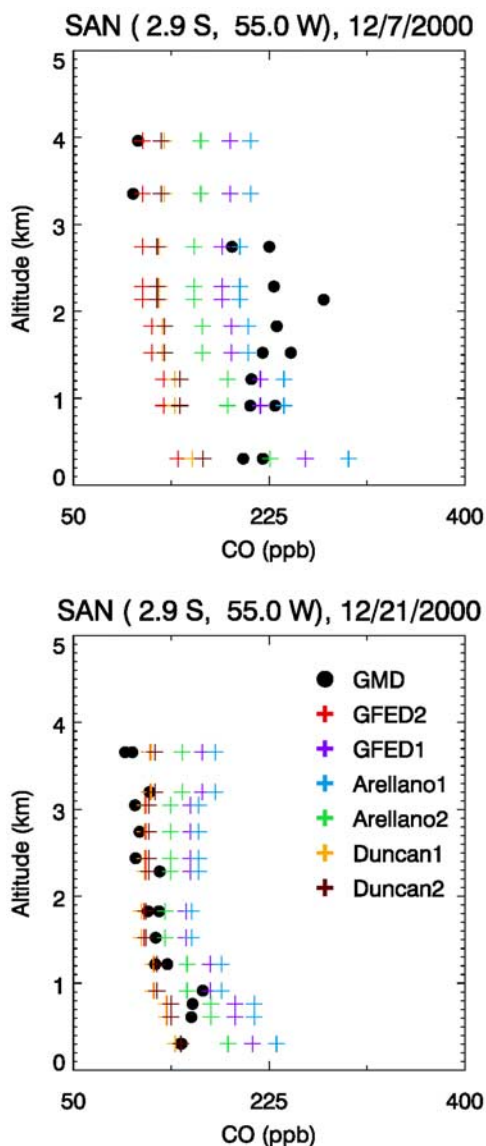
Figure 7. Vertical CO mixing ratio comparisons between model simulations with different biomass burning inventories and CMD aircraft measurements at station SAN on (top) 7 December 2000 (1621–1804 LT) and (bottom) 21 December 2000 (1745–1905 LT).

over the East China Sea. The difference in simulated CO concentrations over central Pacific increases with altitude, indicating that the relative contribution of biomass burning to total CO is larger at higher altitude. Here, CO simulated with two TRMM-based top-down emissions is close to or even larger than that with TOMS-based emissions. This differs with model CO nearer the coast and is attributed to different spatial distributions seen in Figure 4 where TRMM-based emissions are concentrated over Southeast Asia, and TOMS-based emissions also expand to India.

4. Conclusions

[52] We used the Unified Chemistry Transport Model (UCTM) to investigate the sensitivity of global and regional

CO to uncertainties in biomass burning. We examined six commonly used emission inventories (Tables 1 and 2), ranging from 389 to 518 Tg CO/a; this range (i.e., 129 Tg CO/a) represents about 6% of the total source (~2169 Tg CO/a, total direct emissions plus total photochemical oxidation in Table 2). Though 6% may seem small, the regional biomass burning emissions can vary significantly. In Southeast Asia, Central America, Australia, and South America, the emissions from different inventories can differ by more than a factor of four. Consequently, simulated CO in areas close to biomass burning source regions is affected significantly by the choice of emission inventory. For instance, the simulated CO varies by more than 44% of measured CO at the GMD station, Ascension Island, during the biomass burning season of western Africa. Overall, CO is more sensitive to the variation of biomass burning emissions in the SH than in the NH as CO from fossil fuels and biofuels is relatively low in the SH.

[53] To assess quality of these emissions, we compared the simulated CO with measurements from MOPITT, the GMD surface and aircraft network, and the TRACE-P field campaign. Our evaluation indicates that no inventory is better than another on a global scale, but for individual regions clear differences in performance can be identified. This information not only helps in regional model studies, but also provides a starting point for further study to develop a "best" compiled global emission inventory. The strengths and weaknesses of each inventory found in this work are useful to guide future improvements of the inventories.

[54] Globally, the simulation that gives the highest correlation with MOPITT column CO uses the Arellano1 inventory, which is a top-down estimate using GFED1 emissions as a priori and constrained by MOPITT data. However, this inventory gives a higher CO than GMD ground measurements in the high SH austral summer. This may be caused by high SH CO estimation of MOPITT due to the adoption of a global uniform typical vertical CO profile in MOPITT's retrieval. Furthermore, despite the large uncertainty in six biomass burning emissions, all modeled CO concentrations are still within the GMD measured range over the most stations including station Ascension Island which is strongly impacted by fire emissions outflow from the African and South American continents.

[55] Regionally, South America is an area with a significant difference among six biomass burning emission inventories. Inventories of Arellano2, Duncan1 and 2, and particularly GFED2, yield very low CO concentrations. Simulations with Arellano1 and GFED1 are too high. Anomalous high atmospheric CO in Central America is produced by the emissions of Arellano1 and 2 and GFED2, while the other emissions are reasonably good there. In the Southeast Asia biomass burning season, aircraft measurements from the TRACE-P campaign are used to appraise burning emissions independent of the potential large bias from fossil fuel and biofuel emissions. Our analyses indicate that TOMS-based emissions, Duncan1 and 2, are too large, while the TRMM-based bottom-up emissions, GFED1 and 2, are good choices over this region. For NH Africa during boreal winter, the intense fires are easier to detect and the

Table 5. Average Biases Between Modeled and Measured CO From TRACE-P Aircraft Measurements[a]

	GFED2	GFED1	Arellano1	Arellano2	Duncan1	Duncan2
Coast DC8	0.93	0.95	0.96	0.99	1.04	1.06
Coast P-3B	0.88	0.90	0.91	0.93	0.97	0.98
Transit DC8	0.87	0.90	0.91	0.93	0.94	0.97
Transit P-3B	0.90	0.92	0.93	0.95	0.95	0.97

[a]Coast DC8 contains flights in the days of 0303 (3 March), 0307, 0309, 0310, 0313, 0317, 0318, 0320, 0323, 0326, 0329, and 0331. Coast P-3B contains the days 0304, 0307, 0309, 0310, 0313, 0317, 0318, 0321, 0323, 0327, 0330, and 0402. Transit DC8 contains 0227, 0403, 0406, and 0409. Transit P-3B contains 0226, 0227, 0301, 0403, 0406, and 0407.

six sets there are close to each other compared with other fire regions. Fires over SH Africa have two peaks with distinct features. The first peak occurs during May to July over the Democratic Republic of Congo. Emissions of six inventories vary significantly there and none of inventories produce a close simulation of MOPITT CO. There is an overall underestimation of CO concentration during the second peak of SH Africa fires. More work on evaluation of fire satellite products is needed to study this region. In addition, if the evaluation is conducted on an annual basis, the simulated CO over a certain region (for example Central America) may not only be attributed to local fires, but also to the fires that occurred in surrounding areas. Caution should be taken in applying the annual "best" burning performance over certain regions because the good score could be a compromised result of wrong reasons.

[56] The importance of the methodologies and data origins in developing the emission inventories is evident in the similarities between the two TOMS-based emission inventories and between the two top-down emission inventories. It indicates that systematic biases may be persistent in an approach in determining emissions. Intercomparison of CO produced by different emission inventories has shown to be a good method to identify potential systematic errors.
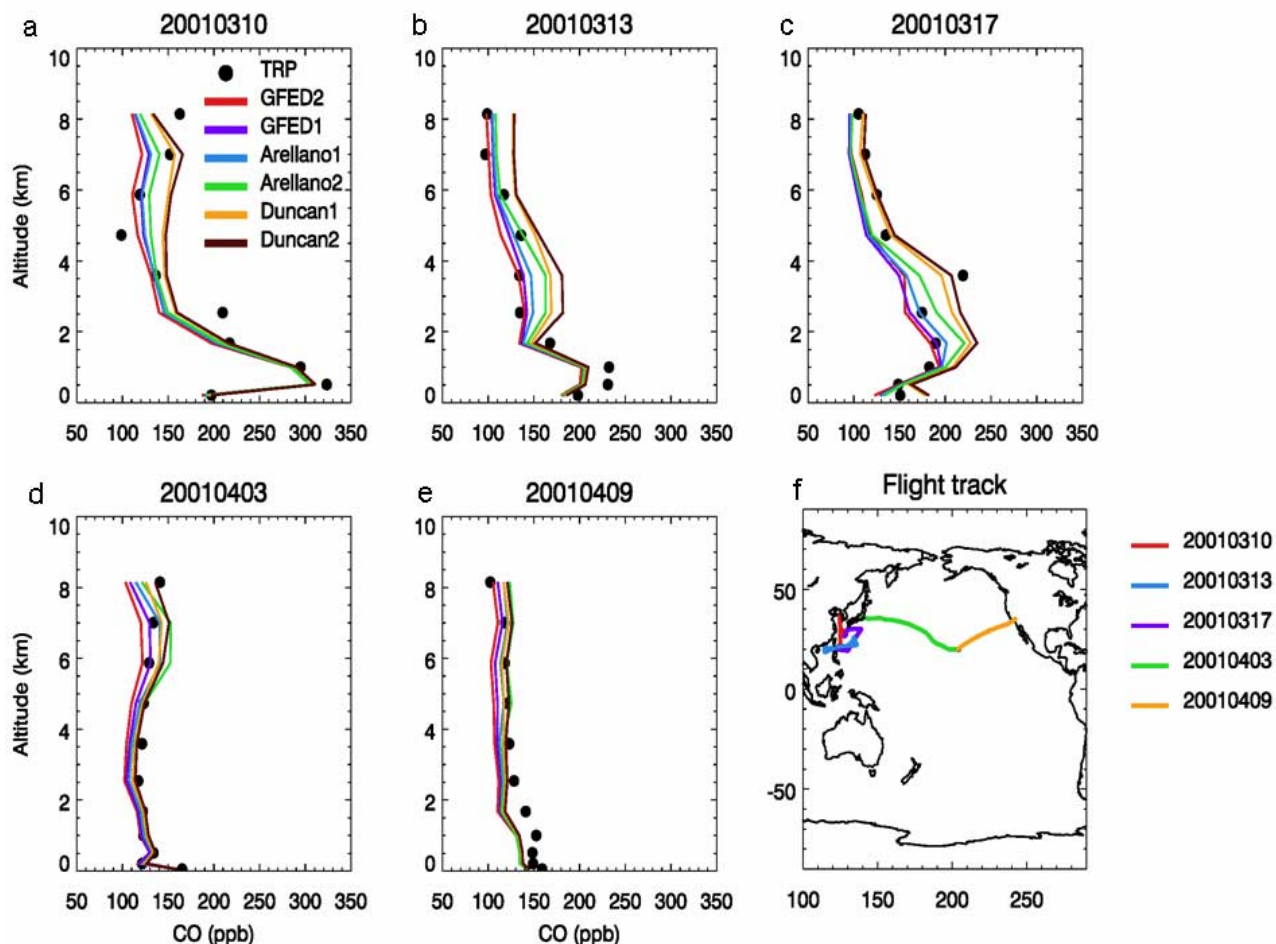
Figure 8. (a–e) Vertical CO profiles simulated by six biomass burning inventories and observed from TRACE-P aircraft measurements. (f) Corresponding flight tracks for these measurements.

References

Allen, D., K. Pickering, and M. Fox-Rabinovitz (2004), Evaluation of pollutant outflow and CO sources during TRACE-P using model-calculated, aircraft-based, and Measurements of Pollution in the Troposphere (MOPITT)-derived CO concentrations, *J. Geophys. Res.*, *109*, D15S03, doi:10.1029/2003JD004250.

Altshuller, P. (1991), The production of carbon monoxide by the homogeneous NOx-induced photooxidation of volatile organic compounds in the troposphere, *J. Atmos. Chem.*, *13*, 155–182.

Arellano, A. F. (2005), Global carbon monoxide cycle: Modeling and data analysis, Ph.D. dissertation, Duke Univ., Durham, N. C.

Arellano, A. F., Jr., and P. G. Hess (2006), Sensitivity of top-down estimates of CO sources to GCTM transport, *Geophys. Res. Lett.*, *33*, L21807, doi:10.1029/2006GL027371.

Arellano, A. F., Jr., P. S. Kasibhatla, L. Giglio, G. R. van der Werf, and J. T. Randerson (2004), Top-down estimates of global CO sources using MOPITT measurements, *Geophys. Res. Lett.*, *31*, L01104, doi:10.1029/2003GL018609.

Arellano, A. F., Jr., P. S. Kasibhatla, L. Giglio, G. R. van der Werf, J. T. Randerson, and G. J. Collatz (2006), Time-dependent inversion estimates of global biomass burning CO emissions using MOPITT measurements, *J. Geophys. Res.*, *111*, D09303, doi:10.1029/2005JD006613.

Bergamaschi, P., R. Hein, C. A. M. Brenninkmeijer, and P. J. Crutzen (2000), Inverse modeling of the global CO cycle: 2. Inversion of ^{13}C/^{12}C and ^{18}O/^{16}O isotope ratios, *J. Geophys. Res.*, *105*, 1929–1945.

Bey, I., D. J. Jacob, R. M. Yantosca, J. A. Logan, B. D. Field, A. M. Fiore, Q. Li, H. Y. Liu, L. J. Mickley, and M. G. Schultz (2001), Global modeling of tropospheric chemistry with assimilated meteorology: Model description and evaluation, *J. Geophys. Res.*, *106*(D19), 23,073–23,078.

Bian, H., S. R. Kawa, M. Chin, S. Pawson, Z. Zhu, P. Rasch, and S. Wu (2006), A test of sensitivity to convective transport in a global atmospheric CO$_2$ simulation, *Tellus, Ser. B*, *58*(5), 463–475.

Bloom, S., et al. (2005), Documentation and validation of the Goddard Earth Observing System (GEOS) Data Assimilation System–Version 4, *NASA/TM-2005-104606, 26*.

Chameides, W. L., P. S. Kasibhatla, J. J. Yienger, H. Levy II, and W. J. Moxim (1994), The growth of continental-scale metro-agro-plexes, regional ozone pollution, and world food production, *Science*, *164*, 74–77.

Chin, M., et al. (2002), Tropospheric aerosol optical thickness from the GOCART model and comparisons with satellite and sun photometer measurements, *J. Atmos. Sci.*, *59*, 461–483.

Chin, M., D. A. Chu, R. Levy, L. A. Remer, Y. J. Kaufman, B. N. Holben, T. Eck, and P. Ginoux (2004), Aerosol distribution in the Northern Hemisphere during ACE-Asia: Results from global model, satellite observations, and Sun photometer measurements, *J. Geophys. Res.*, *109*, D23S90, doi:10.1029/2004JD004829.

Deeter, M. N., et al. (2003), Operational carbon monoxide retrieval algorithm and selected results for the MOPITT instrument, *J. Geophys. Res.*, *108*(D14), 4399, doi:10.1029/2002JD003186.

DeMore, W. B., S. P. Sander, D. M. Golden, R. F. Hampson, M. J. Kurylo, C. J. Howard, A. R. Ravishankara, C. E. Kolb, and M. J. Molina (1997), Chemical kinetics and photochemical data for use in stratospheric modeling, *Eval. 1297-4*, Jet Propul. Lab., Pasadena, Calif.

Douglass, A. R., M. R. Schoeberl, R. B. Rood, and S. Pawson (2003), Evaluation of transport in the lower tropical stratosphere in a global chemistry and transport model, *J. Geophys. Res.*, *108*(D9), 4259, doi:10.1029/2002JD002696.

Duncan, B. N., R. V. Martin, A. C. Staudt, R. Yevich, and J. A. Logan (2003), Interannual and seasonal variability of biomass burning emissions constrained by satellite observations, *J. Geophys. Res.*, *108*(D2), 4100, doi:10.1029/2002JD002378.

Duncan, B. N., J. A. Logan, I. Bey, I. A. Megretskaia, R. M. Yantosca, P. C. Novelli, N. B. Jones, and C. P. Rinsland (2007), Global budget of CO, 1988–1997: Source estimates and validation with a global model, *J. Geophys. Res.*, *112*, D22301, doi:10.1029/2007JD008459.

Emmons, et al. (2004), Validation of MOPITT CO retrievals with aircraft in situ profiles, *J. Geophys. Res.*, *109*, D03309, doi:10.1029/2003JD004101.

Freitas, S. R., K. M. Longo, and M. O. Andreae (2006), Impact of including the plume rise of vegetation fires in numerical simulations of associated atmospheric pollutants, *Geophys. Res. Lett.*, *33*, L17808, doi:10.1029/2006GL026608.

Guenther, A., et al. (1995), A global model of natural volatile organic compound emissions, *J. Geophys. Res.*, *100*, 8873–8892.

Gurney, K. R., et al. (2002), Towards robust regional estimates of CO$_2$ sources and sinks using atmospheric transport models, *Nature*, *415*, 626–630.

Hack, J. J. (1994), Parameterization of moist convection in the National Center for Atmospheric Research community climate model (CCM2), *J. Geophys. Res.*, *99*, 5551–5568.

Hao, W. M., and M.-H. Liu (1994), Spatial and temporal distribution of tropical biomass burning, *Global Biogeochem. Cycles*, *8*(4), 495–504.

Hatakeyama, S., K. Izumi, T. Fukuyama, H. Akimoto, and N. Washida (1991), Reactions of OH with alpha-pinene and beta-pinene in air: Estimate of global CO production from the atmospheric oxidation of terpenes, *J. Geophys. Res.*, *96*, 947–958.

Heald, C. L., et al. (2003), Asian outflow and trans-Pacific transport of carbon monoxide and ozone pollution: An integrated satellite, aircraft, and model perspective, *J. Geophys. Res.*, *108*(D24), 4804, doi:10.1029/2003JD003507.

Heald, C. L., D. J. Jacob, D. B. A. Jones, P. I. Palmer, J. A. Logan, D. G. Streets, G. W. Sachse, J. C. Gille, R. N. Hoffman, and T. Nehrkorn (2004), Comparative inverse analysis of satellite (MOPITT) and aircraft (TRACE-P) observations to estimate Asian sources of carbon monoxide, *J. Geophys. Res.*, *109*, D23306, doi:10.1029/2004JD005185.

Hoelzemann, J. J. (2006), Global wildland fire emission modeling for atmospheric chemistry studies, Ph.D. thesis, Earth Syst. Sci., Max Planck Inst. for Meteorol., Hamburg, Germany.

Hoelzemann, J. J., M. G. Schultz, G. P. Brasseur, C. Granier, and M. Simon (2004), Global Wildland Fire Emission Model (GWEM): Evaluating the use of global area burnt satellite data, *J. Geophys. Res.*, *109*, D14S04, doi:10.1029/2003JD003666.

Holloway, T., H. Levy II, and P. Kasibhatla (2000), Global distribution of carbon monoxide, *J. Geophys. Res.*, *105*, 12,123–12,147.

Ito, A., and J. E. Penner (2004), Global estimates of biomass burning emissions based on satellite imagery for the year 2000, *J. Geophys. Res.*, *109*, D14S05, doi:10.1029/2003JD004423.

Ito, A., and J. E. Penner (2005), Estimates of CO emissions from open biomass burning in southern Africa for the year 2000, *J. Geophys. Res.*, *110*, D19306, doi:10.1029/2004JD005347.

Jacob, D. J., B. D. Field, E. M. Jin, I. Bey, Q. Li, J. A. Logan, R. M. Yantosca, and H. B. Singh (2002), Atmospheric budget of acetone, *J. Geophys. Res.*, *107*(D10), 4100, doi:10.1029/2000JD000694.

Jacob, D. J., J. H. Crawford, M. M. Kleb, V. S. Connors, R. J. Bendura, J. L. Raper, G. W. Sachse, J. C. Gille, L. Emmons, and C. L. Heald (2003), Transport and Chemical Evolution over the Pacific (TRACE-P) aircraft mission: Design, execution, and first results, *J. Geophys. Res.*, *108*(D20), 9000, doi:10.1029/2002JD003276.

Kasischke, E. S., E. J. Hyer, P. C. Novelli, L. P. Bruhwiler, N. H. F. French, A. I. Sukhinin, J. H. Hewson, and B. J. Stocks (2005), Influences of boreal fire emissions on Northern Hemisphere atmospheric carbon and carbon monoxide, *Global Biogeochem. Cycles*, *19*, GB1012, doi:10.1029/2004GB002300.

Kawa, S. R., D. J. Erickson III, S. Pawson, and Z. Zhu (2004), Global CO$_2$ transport simulations using meteorological data from the NASA data assimilation system, *J. Geophys. Res.*, *109*, D18312, doi:10.1029/2004JD004554s.

Kinnison, D. E., et al. (2001), The Global Modeling Initiative assessment model: Application to high-speed civil transport perturbation, *J. Geophys. Res.*, *106*(D2), 1693–1712.

Lamarque, J.-F., and P. G. Hess (2003), Model analysis of the temporal and geographical origin of the CO distribution during the TOPSE campaign, *J. Geophys. Res.*, *108*(D4), 8354, doi:10.1029/2002JD002077.

Lamarque, J.-F., et al. (2004), Application of a bias estimator for the improved assimilation of Measurement of pollution in the Troposphere (MOPITT) carbon monoxide retrievals, *J. Geophys. Res.*, *109*, D16304, doi:10.1029/2003JD004466.

Li, Q., et al. (2002), Transatlantic transport of pollution and its effects on surface ozone in Europe and North America, *J. Geophys. Res.*, *107*(D13), 4166, doi:10.1029/2001JD001422.

Lin, S., and R. B. Rood (1996), Multidimensional flux-form semi-Lagrangian transport schemes, *Mon. Weather Rev.*, *124*, 2046–2070.

Logan, J. A., M. J. Prather, S. C. Wofsy, and M. B. McElroy (1981), Tropospheric chemistry: A glocal perspective, *J. Geophys. Res.*, *86*, 7210–7254.

Manning, M. R., C. A. M. Brenninkmeijer, and W. Allan (1997), Atmospheric carbon monoxide budget of the Southern Hemisphere: Implications of ^{13}C/^{12}C measurements, *J. Geophys. Res.*, *102*, 10,673–10,682.

Mauldin, R. L., et al. (2004), Measurement of OH, HO$_2$/RO$_2$, H$_2$SO$_4$, and MSA during ISCAT 2000, *Atmos. Environ.*, *38*(32), 5423–5437, doi:10.1016/J.atmoshenv.2004.06.031.

Miyoshi, A., S. Hatakeyama, and N. Washida (1994), OH radical-initiated photooxidation of isoprene: An estimate of global CO production, *J. Geophys. Res.*, *99*, 18,779–18,787.

Muller, J.-F., and T. Stavrakou (2005), Inversion of CO and NOx emission using the adjoint of the IMAGES model, *Atmos. Chem. Phys.*, *5*, 1157–1186.

Novelli, P. C., P. M. Lang, K. A. Masarie, D. F. Hurst, R. Myers, and J. W. Elkins (1999), Molecular hydrogen in the troposphere: Global distribution and budget, *J. Geophys. Res.*, *104*, 30,427–30,444.

Orlando, J., B. Noziere, G. Tyndall, G. Orzechowska, S. Paulson, and Y. Rudich (2000), Product studies of the OH- and ozone-initiated oxidation of some monoterpenes, *J. Geophys. Res.*, *105*, 11,561–11,572.

Palmer, P. I., D. J. Jacob, D. B. A. Jones, C. L. Heald, R. M. Yantosca, J. A. Logan, G. W. Sachse, and D. G. Streets (2003), Inverting for emissions of carbon monoxide from Asia using aircraft observations over the western Pacific, *J. Geophys. Res.*, *108*(D21), 8828, doi:10.1029/2003JD003397.

Pan, L., J. C. Gille, D. P. Edwards, P. L. Bailey, and C. D. Rodgers (1998), Retrieval of tropospheric carbon monoxide for the MOPITT experiment, *J. Geophys. Res.*, *103*, 32,277–32,290.

Park, R. J., D. J. Jacob, B. D. Field, R. M. Yantosca, and M. Chin (2004), Natural and transboundary pollution influences on sulfate-nitrate-ammonium aerosols in the United States: implications for policy, *J. Geophys. Res.*, *109*, D15204, doi:10.1029/2003JD004473.

Pétron, G., C. Granier, B. Khattatov, J. Lamarque, V. Yudin, J. Müller, and J. Gille (2002), Inverse modeling of carbon monoxide surface emissions using Climate Monitoring and Diagnostics Laboratory network observations, *J. Geophys. Res.*, *107*(D24), 4761, doi:10.1029/2001JD001305.

Pfister, G., G. Petron, L. K. Emmons, J. C. Gille, D. P. Edwards, J.-F. Lamarque, J.-L. Attie, C. Granier, and P. C. Novelli (2004), Evaluation of CO simulations and the analysis of the CO budget for Europe, *J. Geophys. Res.*, *109*, D19304, doi:10.1029/2004JD004691.

Pfister, G., P. G. Hess, L. K. Emmons, J.-F. Lamarque, C. Wiedinmyer, D. P. Edwards, G. Pétron, J. C. Gille, and G. W. Sachse (2005), Quantifying CO emissions from the 2004 Alaskan wildfires using MOPITT CO data, *Geophys. Res. Lett.*, *32*, L11809, doi:10.1029/2005GL022995.

Prinn, R. G., et al. (2001), Evidence for substantial variations of atmospheric hydroxyl radicals in the past two decades, *Science*, *292*, 1882–1888.

Randerson, J. T., G. R. van der Werf, G. J. Collatz, L. Giglio, C. J. Still, P. Kasibhatla, J. B. Miller, J. W. C. White, R. S. DeFries, and E. S. Kasischke (2005), Fire emissions from C_3 and C_4 vegetation and their influence on interannual variability of atmospheric CO_2 and $\delta^{13}CO_2$, *Global Biogeochem. Cycles*, *19*, GB2019, doi:10.1029/2004GB002366.

Sachse, G. W., G. F. Hill, L. O. Wade, and M. G. Perry (1987), Fast-response, high-precision carbon-monoxide sensor using a tunable diode-laser absorption technique, *J. Geophys. Res.*, *92*, 2071–2081.

Schmitgen, S., H. Geib, P. Ciais, B. Neininger, Y. Brunet, M. Reichstein, D. Lket, and A. Volz-Thomas (2004), Carbon dioxide uptake of a forested region in southwest France derived from airborne CO_2 and CO measurements in a quasi-Lagrangian experiment, *J. Geophys. Res.*, *109*, D14302, doi:10.1029/2003JD004335.

Schultz, M. G. (2002), On the use of ATSR fire count data to estimate the seasonal and interannual variability of vegetation fire emissions, *Atmos. Chem. Phys.*, *2*, 387–395.

Seinfeld, J. H. (1986), *Atmospheric Chemistry and Physics of Air Pollution*, John Wiley, New York.

Shindell, D. T., et al. (2006), Multimodel simulations of carbon monoxide: Comparison with observations and projected near-future changes, *J. Geophys. Res.*, *111*, D19306, doi:10.1029/2006JD007100.

Singh, H., et al. (2000), Distribution and fate of selected oxygenated organic species in the troposphere and lower stratosphere over the Atlantic, *J. Geophys. Res.*, *105*, 3795–3805.

Spivakovsky, C. M., et al. (2000), Three-dimensional climatological distribution of tropospheric OH: Update and evaluation, *J. Geophys. Res.*, *105*, 8931–8980.

Streets, D., et al. (2003), An inventory of gaseous and primary aerosol emissions in Asia in the year 2000, *J. Geophys. Res.*, *108*(D21), 8809, doi:10.1029/2002JD003093.

Streets, D. G., Q. Zhang, L. Wang, K. He, J. Hao, Y. Wu, Y. Tang, and G. R. Carmichael (2006), Revisiting China's CO emissions after the Transport and Chemical Evolution over the Pacific (TRACE-P) mission: Synthesis of inventories, atmospheric modeling, and observations, *J. Geophys. Res.*, *111*, D14306, doi:10.1029/2006JD007118.

Suntharalingam, P., D. J. Jacob, P. I. Palmer, J. A. Logan, R. M. Yantosca, Y. Xiao, M. J. Evans, D. G. Streets, S. L. Vay, and G. W. Sachse (2004), Improved quantification of Chinese carbon fluxes using CO_2/CO correlation in Asian outflow, *J. Geophys. Res.*, *109*, D18S18, doi:10.1029/2003JD004362.

Tan, Q., W. L. Chameides, D. Streets, T. Wang, J. Xu, M. Bergin, and J. Woo (2004), An evaluation of TRACE-P emission inventories from China using a regional model and chemical measurements, *J. Geophys. Res.*, *109*, D22305, doi:10.1029/2004JD005071.

Tie, X., C.-Y. J. Kao, and E. J. Mroz (1992), Net yield of OH, CO, and O_3 from the oxidation of atmospheric methane, *Atmos. Environ., Part A*, *26*, 125–136.

van der Werf, G. R., J. T. Randerson, G. J. Collatz, and L. Giglio (2003), Carbon emissions from fires in tropical and subtropical ecosystems, *Global Change Biol.*, *9*, 547–562.

van der Werf, G. R., J. T. Randerson, G. J. Collatz, L. Giglio, P. S. Kasibhatla, A. Avelino, S. C. Olsen, and E. S. Kasischke (2004), Continental-scale partitioning of fire emissions during the 1997–2001 El Niño/La Niña period, *Science*, *303*, 73–76.

van der Werf, G. R., J. T. Randerson, L. Giglio, G. J. Collatz, P. S. Kasibhatla, and A. F. Arellano Jr. (2006), Interannual variability in global biomass burning emissions from 1997 to 2004, *Atmos. Chem. Phys.*, *6*, 3423–3441.

Vinckier, C., F. Compernolle, A. M. Saleh, N. Vanoof, and I. Vanhees (1998), Product yields of the alpha-pinene reation with hydroxyl radicals and the implication on the global emission of trace compounds in the atmosphere, *Fresenius Environ. Bull.*, *7*(5–6), 361–368.

Wang, Y., D. J. Jacob, and J. A. Logan (1998), Global simulation of tropospheric O_3-NOx-hydrocarbon chemistry: 1. Formulation, *J. Geophys. Res.*, *103*, 10,713–10,725.

Wang, Y. X., M. B. McElroy, T. Wang, and P. I. Palmer (2004), Asian emissions of CO and NOx: Constraints from aircraft and Chinese station data, *J. Geophys. Res.*, *109*, D24304, doi:10.1029/2004JD005250.

Yevich, R., and J. A. Logan (2003), An assessment of biofuel use and burning of agricultural waste in the developing world, *Global Biogeochem. Cycles*, *17*(4), 1095, doi:10.1029/2002GB001952.

Zhang, G. J., and N. A. McFarlane (1995), Sensitivity of climate simulations to the parameterization of cumulus convection in the Canadian climate center general-circulation model, *Atmos. Ocean*, *33*, 407–446.

———————————

A. Arellano, National Center for Atmospheric Research, Boulder, CO 80307, USA.

H. Bian and B. Duncan, Goddard Earth Sciences and Technology Center, University of Maryland, Baltimore County, Baltimore, MD 21228, USA. (bian@rondo.gsfc.nasa.gov)

M. Chin and S. R. Kawa, Atmospheric Chemistry and Dynamics Branch, NASA Goddard Space Flight Center, Greenbelt, MD 20771, USA.

P. Kasibhatla, Nicholas School of the Environment and Earth Sciences, Duke University, Durham, NC 27708, USA.